

Received April 27, 2020, accepted June 16, 2020, date of publication July 6, 2020, date of current version August 12, 2020.

Digital Object Identifier 10.1109/ACCESS.2020.3007565

3D Printed Low-Cost Force-Torque Sensors

NORMAN HENDRICH¹, **FLORENS WASSERFALL,**
AND JIANWEI ZHANG, (Member, IEEE)

Informatics Department, University of Hamburg, 22527 Hamburg, Germany

Corresponding author: Norman Hendrich (hendrich@informatik.uni-hamburg.de)

This work was supported in part by the German Research Foundation (DFG) in project Crossmodal Learning under Grant SFB TRR 169.

ABSTRACT Force sensing is essential for many manipulation tasks and, more generally, for all robots physically interacting with their environment. While multi-axis force/torque sensors are readily available commercially, their cost and complex integration have so far limited a wide deployment. In this paper, we introduce a modular approach to design and to integrate low-cost force sensors directly into 3D printed robot parts. Based on off-the-shelf optical sensors embedded into deformable structures, sensitivity and load capacity can be selected from a wide range. A working six-axis sensor, including electronics, can be built for less than 20 dollars, plus a few hours of 3D printing. We present tested example designs for sensors of different complexity, from a basic one-dimensional deflecting beam to six-axis sensors with custom shapes. We summarize the basic sensor layout geometries, explain key 3D printing and integration aspects, discuss sensor calibration, and describe our Arduino firmware and ROS-based drivers.

INDEX TERMS Force and tactile sensing, force-torque sensor, optical force sensing, 3D printing, fused-filament fabrication (FFF), sensor calibration, LASSO, huber regression.

I. INTRODUCTION

As noted by Cutkowsky *et al.* [1], force and tactile sensing has been an active research area for robotics almost as long as computer vision, but it “always seems to be a few years away from widespread utility.” As there can be little doubt about the central role of force and tactile sensing for human manipulation and many robot assembly tasks, the problem then is in the availability of suitable sensing technologies, their robustness, and, last but not least, costs.

In this paper, we propose and demonstrate a family of 3D printed force and torque sensors using off-the-shelf optical sensors (Fig. 1). While the basic sensing principle is well-known, the mechanical alignment of multiple optical sensors required for multi-axis force and torque decoupling can be surprisingly difficult. We present and discuss simple and proven designs that can be built with common FFF/FDM (fused filament fabrication, fused deposition modeling) 3D printers. The contributions of this paper include:

- a brief summary of optical sensors and the electronics required for readout,
- an overview of mechanical structures and sensor layouts for multi-axis force and torque decoupling,









The associate editor coordinating the review of this manuscript and approving it for publication was Rui-Jun Yan¹.



FIGURE 1. A family of 3D printed low-cost force-sensing objects, based on proximity- or interrupter-type optical sensors (inset on bottom left). The examples in the figure range from a 2-DOF friction-force sensor for object pushing experiments to 6-DOF force/torque sensors with different sizes, shapes, and sensitivity. Also shown is a 17-DOF force/torque-sensing screwdriver for learning from human demonstration.

- proven example 3D printable sensor structures with user-selectable per-axis stiffness,
- planar proximity sensor configurations combined with printed grayscale patterns for six-axis decoupling,

TABLE 1. Key parameters of the presented force/torque sensors.

	Sensor	DOF	Size [x,y,z] [mm]	Payload [N, Nm]	Sensors number, type	ADC channels, bits	Parts microcontroller	Qty	Cost	Sum
	Foot-Sensor	4x1	50, 10, 5	50 N	1x reflex	4x13	Teensy 3.2 ITR 8307	1 4	24 \$ 50 ¢	26 \$
	Pushing-FT	2	50, 50, 12	0.05 N	2x fork	2x10	Arduino Nano (clone) Vishay 1103	1 2	5 \$ 1 \$	7 \$
	Screwdriver handle tool mount	6x2 5	5, 13, 50 ϕ 50, h 17	20 N 3 Nm	12x reflex 5x reflex	muxed 6x2 5	Nano 33 IOT (WiFi) ITR 8307 ITR 8307	1 12 5	30 \$ 50 ¢ 50 ¢	39 \$
	Spacemouse (fork, thin hat)	6	ϕ 42, h 35	2 N	6x fork	6x13	Teensy 3.2 Vishay 1103	1 6	24 \$ 1 \$	30 \$
	Spacemouse (reflex, thick hat)	6	ϕ 42, h 50	4 N	6x reflex	6x13	Teensy 3.2 ITR 9904	1 6	24 \$ 1 \$	30 \$
	Adjustable-FT	6	ϕ 104, h 42	20 N	8x fork	8x10	Arduino Nano (clone) Vishay 1103	1 8	5 \$ 1 \$	13 \$
	Block-FT	6	56, 56, 36	11 N	8x reflex	8x10	Arduino Nano (clone) ITR 8307	1 8	5 \$ 50 ¢	9 \$
	Bottle-FT (ring-type)	6	ϕ 114, h 25 ϕ inner 70	10 N	8x fork	8x10	Arduino Mini (clone) Vishay 1103	1 8	5 \$ 1 \$	13 \$
	ATI Nano-17	6	ϕ 17, h 15	12 N	6x strain-gauge	external	-	1	5000 \$	
	Sunrise M3207	6	ϕ 74, h 17	500 N	6x strain-gauge	external	-	1	4000 \$	

- a modular sensor concept that combines a fixed sensor carrier with different elastic “hats” of different stiffness,
- guidelines and structures for the critical mechanical alignment of multiple optical sensors,
- a collection of 3D printed example designs with explanations of the design decisions and lessons learned.

Advantages of the presented modular concept include the potential to design sensors and systems exactly for the task at hand, the fast prototyping cycle due to 3D printing, and the ease of system integration, both mechanically and electrically. Total sensor costs are usually dominated by the microcontroller used.

The key parameters of our prototype sensors are summarized in Table 1. As can be seen, all presented sensors are designed for light to medium loads. While optical sensing can, of course, be combined with metal mechanical structures, the cost advantage diminishes, and established technologies are still preferred when high payloads, high accuracy, or high overload capacity are required. The sensors proposed here are also less stiff than strain-gauge sensors, which can be either a benefit or a drawback — depending on the application.

This paper is organized as follows. Section II first reviews related research on force sensing in general and recent work on 3D printed sensors in particular. Section III summarizes the characteristics of optical proximity and fork-type sensors, lists possible geometries for multi-axis sensors, and recaps beam deflection concepts from elasticity theory. Section IV describes our open-source software tools, including OpenSCAD utilities, Arduino firmware, and ROS drivers. Several approaches to sensor calibration are also discussed. A portfolio of actual sensor prototypes is presented in section V, with an explanation of key design decisions as

well as specific 3D printing and assembly aspects. The paper concludes with an outlook on future work.

II. RELATED WORK

Industrial 3-DOF and 6-DOF *strain-gauge force/torque sensors* are readily available in a wide range of sizes and maximum forces [2], [3]. Such sensors are factory calibrated with low drift and noise, provide high mechanical stiffness and overload protection, and enable industrial robots for tasks requiring force or impedance control. Unfortunately, the costs of these sensors remain high, and the required precision amplifiers and electronics make integration into smaller and mobile robots a challenge.

Regarding *force and tactile sensing* in general, a variety of sensor technologies have been studied to measure normal forces applied to a robot part or surface, including resistive and piezoresistive materials [4], [5], conductive rubber [6] and polymers [7], magnetic [8] and capacitive sensors [9], and several variants of optical sensing [10]. In addition to single sensors, array sensors have been proposed for most of the approaches, e.g. [11] [12]. The design of force and tactile sensors for robot hands capable of dexterous manipulation remains an unsolved challenge [13]–[15].

For *multi-axis force/torque sensors*, the search for compact structures attracted a lot of work [16]–[18]. In [19], optimal strain-gauge placements are calculated from a set of optimality criteria. Usually, simple geometric forms are preferred, e.g., the cross for three-axis (F_z, M_x, M_y) sensors, and two concentric rings connected by thin arms for six-axis sensors [20], [21]. Recently, multi-stage constructions combining low- and high-rigidity elements were proposed to increase the dynamic range of the sensors [22]–[24]. As deflections are quite small in strain-gauge sensors, linear behavior can

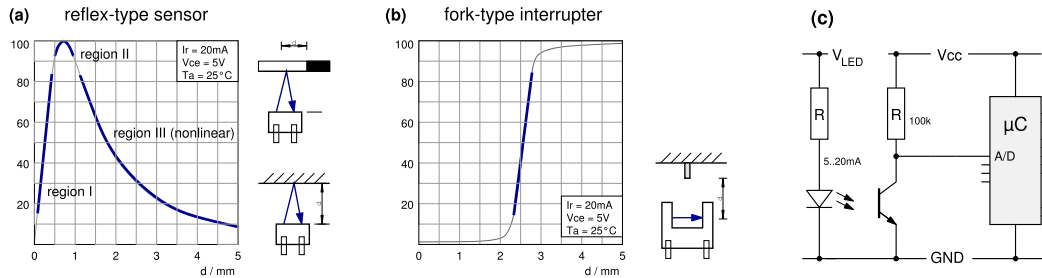


FIGURE 2. Basic characteristics of optical light sensors. (a) Typical response of reflex-type (proximity) sensors. (b) Typical response of fork-type (interrupter) sensors. (c) Basic sensor readout circuit using a microcontroller.

be assumed, and the decoupling matrices correspond to the mechanical structure. Decoupling using a special neural network was proposed in [25].

The use of *optical photointerrupters* for force sensors was first proposed in [26] and demonstrated with a complete six-axis sensor design. Apart from the lower cost, immunity to electrical noise is another advantage. Later work focused on simpler layouts, including a 1-DOF optical robot joint torque sensor (M_z) [27]. A force sensor for a tendon-driven robotic hand with 200 N payload integrated into the distal phalanx of the finger was presented in [28]. Different elastic elements and sensor configurations of a 3-DOF force/torque sensor (F_z, M_x, M_y) were analyzed in [29]. Another 3-DOF sensor for a walking-assist robot, based on four photointerrupters in the common cross-type layout, was proposed in [30].

Force sensing using optical *reflex-type sensors* has also been studied. A tactile fingertip (F_x, F_y, F_z) was reported in [31], followed by a shearing force measuring fingertip combining 40 photodiodes [32]. Another robust three-axis force sensor using three photodiodes and a reflecting rubber sphere was demonstrated in [33], and a fingertip force sensor based on a 5x5 matrix of reflex-type sensors combined with a soft cover is reported in [34].

Based on a geometric analysis of light reflection in a proximity sensor, [35] formulated recommendations for function approximation, including polynomials and multilayer perceptrons. A full six-axis force/torque sensor composed of three planar sensor modules with 4 photodiodes each, arranged at three sides of a cube, was proposed in [36].

Regarding *3D printing*, material properties like modulus of elasticity and ultimate stress are discussed in standard textbooks, e.g. [37], [38]. However, due to the filament deposition and the layered structure, FFF-printed objects show strong anisotropic behavior along and orthogonal to the extrusion paths and between layers. Several studies focused on the mechanical properties of FFF-printed ABS and PLA objects [39]–[41], while the geometric accuracy of FFF-printed objects was analyzed in [42].

A guideline for the *rapid prototyping* of force sensors [43] described a 1-DOF force sensor based on fiber optics. Another very sensitive 3D printed optical force sensor based on Fiber Bragg wavelength shift was presented recently [44]. The works most similar to ours are a 1-DOF torque sensor

FFF-printed from ABS plastic [45] and the 3D printed force sensor described in [46], [47]. Relying on high-end 3D printing technology, the latter sensor is quite small and provides 3-axis (F_z, M_x, M_y) force measurements. Stacking two of these sensors, the same group realized a 5-DOF force/torque sensor [48].

III. CONCEPT

The (well known) principle of the proposed force sensors is based on elastic cantilever structures, where the deformation under load is measured in turn by contactless optical sensors. We first review the characteristics of the optical sensors and list the basic geometries for multi-axis decoupling. We discuss the design of cantilever structures with axis-specific stiffness, and explain the use of spiral springs as the key elastic elements in our force sensors.

A. OPTICAL PROXIMITY SENSORS AND PHOTOINTERRUPTERS

Optical *proximity sensors* combine an infrared LED and a phototransistor mounted side by side (e.g. [49], [50]). When a reflecting surface is close (0.5..4 mm) to the sensor, some light is reflected into the phototransistor inducing a current.

These sensors are typically used to measure either the distance (z -axis) to a fully reflective surface above the sensor, or the overlap with a black/white pattern moving along the x -axis at constant z -height. See figure 2a for a sketch of typical sensor response. The annotation shows three main operating regions with different behavior. In region I, sensor current increases quickly and almost linearly to the maximum over a z -distance of about 0.5 mm, useful for optical end-stop applications. The transition region II covers the distance of maximum reflection and can be used with black/white patterns (at fixed z) to measure the x -deflection. In region-III, the sensor current finally falls off over a z -distance of a few millimeters, but the response to the distance is nonlinear.

Optical *photointerrupters* combine an infrared LED and a phototransistor in a fork-type arrangement (e.g. [51]). The light beam is blocked when an opaque object moves into the slit, again changing the phototransistor current. As those sensors are often used for optical end-stop applications, the light beam is quite thin, with a sharp transition from light to

dark over (typically) less than 0.3 mm (Fig. 2b). The center part of the transition curve is almost linear with distance.

Both sensor types are usually designed for infrared light with wavelengths in the range of $\lambda = 700 \dots 1400$ nm to reduce interference from daylight, but the sensors are still sensitive to sunlight and other infrared radiation sources. Depending on the application and environment, extra optical shielding of the phototransistors may be necessary.

B. ELECTRONICS

The basic circuit for optical sensor readout consists of just four components, with the emitter LED connected to a stable power supply via a series resistor that sets the LED current. Using another pull-up (or pull-down) resistor, the phototransistor current is easily converted to a voltage that can be measured directly by the built-in analog-digital converters of common microcontrollers (Fig. 2c).

Exploiting this, our sensors are designed around popular *microcontroller boards* like Arduino [52] and Teensy [53]. These boards are readily available at low cost and come with full documentation and good software support, including bootloaders for reprogramming via USB. As the boards already provide high current digital output pins, multi-channel analog-digital converters, and standard serial communication interfaces, very few external components are required. The form factor of these boards is also small enough to permit integrating all electronics directly into the sensor housing, eliminating the need for expensive shielded analog cables between sensor and amplifier.

A *stable power supply* is essential for the proposed application, as the forward current of the LEDs (and, therefore, emitted light) increases steeply with applied voltage. Most Arduino-style boards support dedicated external power supplies, but can also be run as USB bus-powered devices. While convenient, requiring only a single cable for power and data communication, USB power from a PC may significantly limit sensor accuracy, as the voltage may change over time due to power management and the activity of other devices on the USB bus. If the additional communication latency can be tolerated, a USB hub powered by an external high-quality power supply provides a working solution.

The typical voltage drop across an infrared LED is about 1.2 V, so that two or three LEDs can be connected in series at 3.3 or 5 V supply voltage. Given typical forward currents in the range of 5...20 mA, total current consumption for a sensor with eight LEDs is about 80 mA for continuous operation. When necessary, e.g. for battery-operated devices, the LEDs can also be pulsed, reducing average power according to the duty-cycle. Also, it may be possible to share the signal outputs of multiple phototransistors, reducing the number of required A/D converter inputs.

Multiple factors limit *sensor resolution*, mainly the onboard A/D converter, the voltage swing generated by the optical sensor, and the stability of the power supply. If necessary, custom circuit boards can be designed with multi-channel high-resolution A/D converters, suitable

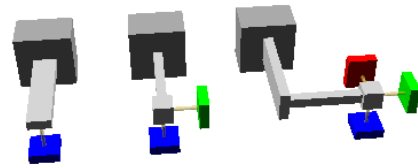


FIGURE 3. Multi-axis motion sensing with optical reflex sensors. (a) one distance sensor (F_z), (b) two orthogonal distance sensors (F_y, F_z), (c) the end of the angled beam can deflect in three directions, three sensors (F_x, F_y, F_z).

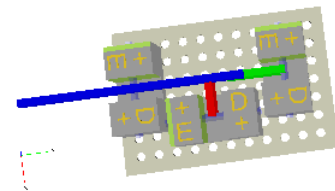


FIGURE 4. Planar layout for three-axis motion sensing with fork-type sensors. Initially, the lever shades half of all three light beams. Small translations modulate the light of only the corresponding sensors.

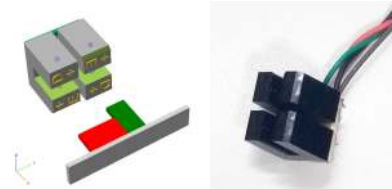


FIGURE 5. The proposed 2-DOF sensor module and the combined stacked fin whose lower part (red) shades the left sensor to measure x -axis deflection, while the taller part (green) shades the right sensor to measure the y -motion.

signal pre-amplification [47], and advanced LED current stabilization.

Recently, integrated *digital proximity sensors* have become available that combine an infrared LED, the phototransistor, a matched analog-digital converter, and digital control in a single chip [54], [55]. While more expensive than the basic proximity sensors, these devices provide current control for the emitter LEDs and support pulsed operation for dark-current detection and power saving. Standard I²C multiplexers can be used to address six or eight of these devices as required for a multi-axis force/torque sensor.

C. THREE-AXIS MOTION DECOUPLING

The characteristics of the two kinds of optical sensors immediately suggest possible layouts to decouple axis-specific motion in multi-sensor setups. For proximity sensors, the output current induced by a uniform reflective surface above the sensor changes with z -distance but is independent of the surface x - and y -translation. One, two, or three proximity sensors are therefore sufficient to decouple and measure motion along the x , y , and z -axes (Fig 3).

Assuming that the sensors are aligned to operate in the linear part of their characteristic curves around the null position o_i , the output of sensor S_i can be approximated as

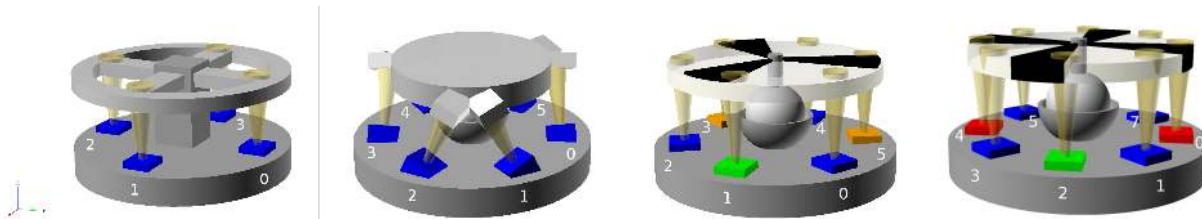


FIGURE 6. Geometries for multi-axis force and torque decoupling. (a) Cross-type layout, four distance sensors (F_z, M_x, M_y). (b) Stewart platform, six tilted distance sensors; six-axis measurement of ($F_x, F_y, F_z, M_x, M_y, M_z$). (c) Planar six-axis layout with three distance sensors (blue: measuring z) and three black/white pattern sensors measuring x/y -deflection (green: y , orange: combined x/y); (d) Redundant planar layout with four distance sensors (blue: z) and four pattern sensors (red: x , green: y).

$S_i(z) = g_i \cdot (z - o_i)$ with some gain factor g_i . The basic decoupling equations for the setups shown in figure 3 are:

3a: $F_z = S_1(z)$.

3b: $F_y = S_1(y), F_z = S_2(z)$.

3c: $F_x = S_1(x), F_y = S_2(y), F_z = S_3(z)$.

For fork-type sensors, even a planar sensor arrangement can achieve 3-axis motion decoupling (Fig. 4). In the layout, the moving lever obstructs the light beams of three sensors mounted on the circuit board. The parts of the lever marked in red and green enter a light-beam sideways to measure deflection in the x - and y -direction, while the blue part enters the third light-beam from above, measuring the z -motion.

D. 2-DOF SENSOR MODULE

Standard sized interrupter devices feature a slot width of about 3 mm, and the depth from the top of the sensor housing to the light beam is also around 3 mm. Given the need for an unobstructed lever motion of about ± 1 mm in all three axes, rather thin and long “fins” are needed. Unfortunately, creating thin tall structures is difficult in FFF 3D printing.

Therefore, we propose an arrangement of two fork-type sensors next to each other, forming a “2-DOF sensor module” (Fig. 5). A single staggered fin protrudes into the combined slot from the front (x) and the inside (y) of the light beams. This way, no extra free space is required outside the combined slot of the two sensors, and the fins are sturdy enough for reliable 3D printing on typical FFF machines. These 2-DOF modules have been used successfully in several of our prototypes (compare sections V-B, V-E, V-G below).

Electrically, the combination of two photointerrupters also makes sense, as ground can be shared and the two infrared LEDs can be connected in series. The LED series resistor and optional pull-ups can be integrated on the module, resulting in a clean 4-wire interface to the microcontroller (GND, LED power, 2x phototransistor).

E. GEOMETRIES FOR MULTI-AXIS DECOUPLING

At least n sensors are required to measure and decouple motions from n independent degrees of freedom, but a larger number of sensors might be used when appropriate, e.g. to use axis-aligned sensors or to exploit redundancy.

In principle, all common geometries developed for strain-gauge sensors could be used [2], [3]. However, the larger deflections needed for optical sensors influence the choice of the most suitable structures (Fig. 6). The popular layout shown in Fig. 6a realizes a 3-DOF force/torque sensor, combining four z -distance sensors to measure F_z, M_x, M_y . Counting sensors clockwise from the rightmost ($+y$) sensor S_0 :

6a: $F_z \sim (S_0 + S_1 + S_2 + S_3)$

$M_x \sim (S_0 - S_2) \quad M_y \sim (S_1 - S_3)$

A six-axis sensor that fully decouples forces and torques ($F_x, F_y, F_z, M_x, M_y, M_z$) needs at least six optical sensors with different orientations, e.g. tilted in a Stewart platform arrangement (Fig. 6b). For this geometry, the actual coefficients depend on the exact location and tilt angle of the sensors. In the example:

6b: $F_x \sim (S_0 + S_1 + S_2 + S_3) - (S_4 + S_5)$

$F_y \sim (S_1 + S_4) - (S_2 + S_5)$

$F_z \sim (S_0 + S_1 + S_2 + S_3 + S_4 + S_5)$

$M_x \sim (S_0 + S_1 + S_5) - (S_2 + S_3 + S_4)$

$M_y \sim (S_1 + S_2) - (S_4 + S_5)$

$M_z \sim (S_0 + S_2 + S_4) - (S_1 + S_3 + S_5)$

A planar configuration can be achieved by combining sensors looking upwards at a uniform surface (measuring z) with sensors looking at black and white patterns measuring x and y motion (Fig. 6c and d). Again, the basic decoupling equations are then derived from the geometries:

6c: (green sensor S_1 aligned with $+x$):

$F_x \sim (S_3 - S_5) \quad M_x \sim (S_0 - S_2)$

$F_y \sim S_1 - \frac{1}{2}(S_3 + S_5) \quad M_y \sim \frac{1}{2}(S_0 + S_2) - S_4$

$F_z \sim (S_1 + S_3 + S_5) \quad M_z \sim (S_0 + S_2 + S_4)$

6d: (rightmost sensor S_0 aligned with $+y$):

$F_x \sim (S_0 - S_4) \quad M_x \sim (S_1 + S_7) - (S_3 + S_5)$

$F_y \sim (S_2 - S_6) \quad M_y \sim (S_1 + S_3) - (S_5 + S_7)$

$F_z \sim (S_1 + S_3 + S_5 + S_7) \quad M_z \sim (S_0 + S_2 + S_4 + S_6)$

More complex equations arise when using proximity sensors in their nonlinear regime (region-III), e.g. when fitting higher-degree polynomials. However, as described below in section IV-D, we rely on machine-learning approaches to estimate the sensor calibration matrices directly instead of first deriving coupling equations.

F. ONE-DIMENSIONAL BEAM DEFLECTION

The optical sensors described above need reflector/obstacle motions of about 0.2 . . . 3 mm for full signal swing — much larger than the typical deflections of a few μm needed for strain-gauges or capacitive sensors [1]. The mechanical structure of the proposed sensors must include elements that tolerate such elastic deflection without permanent deformation or breakdown.

The deflection ω(x) of a thin cantilever loaded with forces q(x) is described by the static Euler-Bernoulli beam equation,

$$\frac{d^2}{dx^2} \left(EI \frac{d^2\omega}{dx^2} \right) = q(x) \tag{1}$$

where E describes Young’s modulus and I is the beam’s second moment of area. Solving the differential equation gives the deflection s of a single-suspended thin elastic beam under a force F applied at the sensor position l,

$$s = \frac{l^3 F}{3EI}, \quad \text{with } l \cdot F = \text{bending moment } M. \tag{2}$$

The moment of inertia of a rectangular beam of width b and height h is given by I = (bh³)/12. Combining both equations, the deflection of a thin rectangular beam (l ≫ h) with one fixed support is given by

$$s = \frac{l^3 F}{3EI} = \frac{4}{E} \cdot \frac{l^3}{b \cdot h^3} \cdot F, \tag{3}$$

proportional to the applied force F, with a cubic dependency on beam length, inverse cubic on beam height, and an inverse dependency on beam width. Similarly, the deflection s of a cantilever of length l with two fixed supports under center load F is given by [38]

$$s = \frac{l^3 F}{192EI} = \frac{1}{16E} \cdot \frac{l^3}{b \cdot h^3} \cdot F \tag{4}$$

again resulting in a cubic dependency on beam length and height. By careful selection of those dimensions, the required deflections of a few millimeters can easily be reached in devices of moderate size. When using 3D printing, additional constraints like minimum feature size may apply. In FFF technology, the cantilever width b (and to some degree, also the height h) should be larger than the extrusion width e of the printer, and typically is selected as a multiple of the extrusion width, so that the slicing software can generate continuous extrusion paths along the cantilever.

G. CUSTOM BEAM ARRANGEMENTS

While the simple angled cantilever beam shown in Fig. 3 already provides the deflection in all three coordinate axes

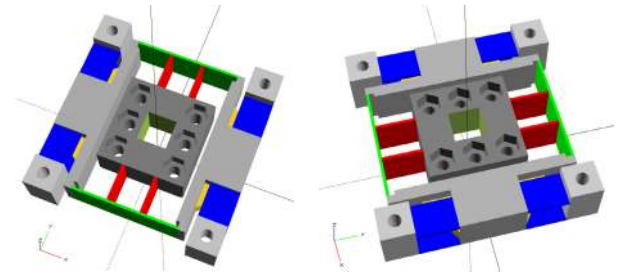


FIGURE 7. Example elastic member with user-selectable per-axis stiffness. The structure consists of the rigid core and three sets of orthogonal elastic bars, connected by rigid intermediates. In the example, the thin inner bars (red) provide x-axis motion, but are stiff against forces in the y- and z-directions. The same applies to the middle bars (green) for the y-axis and the outer bars (blue) for the z-direction. By individual dimensioning of the bars and their spacing, the sensitivities (F_x, F_y, F_z, M_x, M_y, M_z) can be selected independently.

TABLE 2. Axis-specific stiffness: example parameters and corresponding deflections for the structure shown in Fig. 7. n: number of beams (per direction), s_x, s_y, s_z beam size along axis, d distance between pairs, Δx, Δy, Δz resulting deflection (in millimeters) under a force of 10 N.

	n	dimensions			d	deflection 10 N force		
		s _x	s _y	s _z		Δx	Δy	Δz
x-beams	4	0.7	11	10	12	1.94	0.03	0.02
y-beams	4	9	0.7	10	30	0.01	1.62	0.005
z-beams	8	8	10	0.7	30	0.002	0.007	0.91

required for multi-axis force/torque sensing, more complex mechanical structures may be needed when designing sensors for specific applications. The mechanical properties of an arbitrary sensor geometry could be approximated by finite elements analysis (FEM), but this approach requires considerable user expertise and computational effort. Also, FFF-printed objects show significant anisotropy due to the layered process, and the final printing toolpath generated during slicing is hard to import into FEM tools.

However, at least an initial estimation of the expected deflection under applied loads can often be derived from the basic one-dimensional cantilever bending model. The beam dimensions can then be scaled and adjusted to reach the required force range for the application at hand without any deeper understanding of elasticity theory.

For example, the elastic structure shown in Fig. 7 allows 3D deflection of the outer part (four outer bores) with respect to the inner core. Due to the orthogonal arrangement of thin but tall levers, forces applied along the (x, y, z)-axes predominantly deflect the weakest pair of levers, colored accordingly in red, green, blue (Table 2). Dimensioning the levers accordingly then allows us to select the force range along the principal axes independently from each other.

A torque will again mostly deflect the axis-specific set of levers, but the resulting deflection now also depends on the spacing between the relevant levers. In the example, the spacing is large for the y- and z-levers, but quite small for the x-sensitive levers (red). Accordingly, this structure will feature similar deflections for F_x and F_y, about half the deflection for F_z (eight levers instead of four), similar torque limits

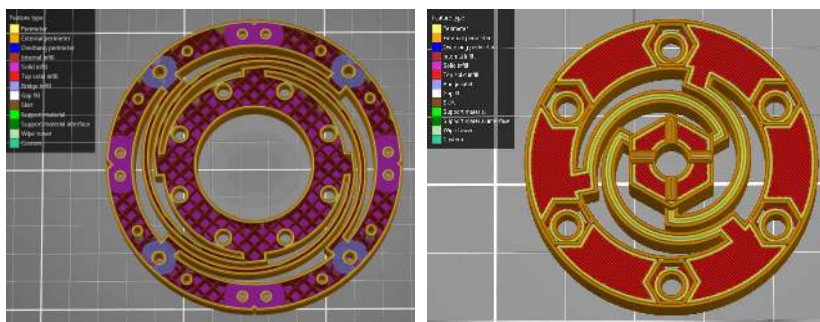


FIGURE 8. Planar spiral springs provide deflection in (x, y, z) and can be 3D printed on FFF printers without support structures. Continuous extrusion paths without sharp corners are crucial to avoid early fracture. (a) large version, $d = 104$ mm, $F_x, F_y = 20$ N, $F_z = 25$ N, inner screw bores match robot mount (section V-E). (b) small spring, $d = 45$ mm, effective $F_x, F_y, F_z = 4$ N, (section V-D).

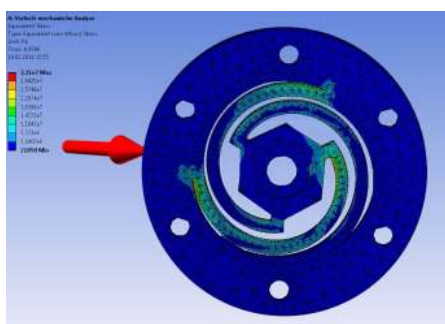


FIGURE 9. FEM analysis of a spiral spring. The figure shows the mechanical stress under applied force $F = (F_x, F_y, F_z) = (10, 0, 10)$ N (red arrow) on the left part of the outer ring.

for M_x and M_z , but a very low torque limit for M_y due to (probably unwanted) torsion of the x -levers in addition to the (expected) deflection of the z -levers.

H. SPIRAL SPRINGS

Given that 3D printing technology can easily create non-rectangular shapes, spiral springs are an efficient solution to the problem of finding a compact elastic structure whose ends can deflect in all three axes (Fig. 8). The theory of flat and helical spiral springs has long been studied and analytical results are known for rectangular and circular cross-sections [56]–[58] and for special applications like clock hairsprings and constant-torque mainsprings [59]. The usage of spiral springs in a multi-axis joystick with optical readout was patented in [60].

However, the theoretical models are quite complex and several of the assumptions (e.g. homogeneous material) are not fulfilled for FFF 3D printing. As a first approximation, the deflection of the spiral arm in the x - and y -direction can be estimated by projection onto the corresponding axes and using the resulting length l with known height h and width b of the arm, and using the total arm length for z deflection.

Still, a finite-element analysis might be needed for accurate dimensioning and stress analysis of such spring

structures [61]. The example analysis shown in Fig. 9 predicts peaks of mechanical stress concentration in the acute angles between the spiral arms and the outer ring; our actual FFF-printed specimen of this design failed quickly due to extrusion delamination near those points. The improved design (Fig. 8b) uses lower curvature to reduce this problem.

I. OVERLOAD PROTECTION

Unlike most metals, common 3D printed plastics have a much lower overloading tolerance beyond the elastic regime, and parts will break quickly instead of first deforming. Due to the layered structure, FFF-printed parts are also prone to layer delamination in areas of local stress concentration [39], [40]. On the other hand, the latter study also flexed 3D printed cantilevers below the load limit without problems for up to a million load cycles in fatigue testing.

Most of our sensors include mechanical end-stops for the elastic parts, ensuring that a safe deflection is never exceeded. For example, the spacing of the arms in the spiral springs is selected so that neighboring arms will touch each other under large loads, reducing the effective beam length l and greatly increasing stiffness against further deflection. Of course, the sensor software should warn about the overload condition if such end-stops are reached during regular operation.

As overload conditions cannot always be avoided, fracture of elastic parts must be considered when designing the sensors. Unfortunately, the fracture of one spring element increases the load on the remaining parts, with a high risk of successive cracks and complete failure of the structure. It is good practice to ensure robust caging of the moving parts of the force/torque sensors so that any external tools mounted to the sensor will be caught safely instead of falling down. Caging can often be achieved with little overhead, as the mounting parts are typically already much stronger than the intentionally thin deflecting beams.

For example, broken elastic arms in the spiral springs discussed above will usually leave the much stronger inner core and outer rings intact, protecting against any excess motion in the x, y -plane. Motions towards $-z$ are similarly blocked by

the base of the sensor, so that only a single extra catching element for the $+z$ direction (e.g. a collar attached to the inner core) must be provided. The quarter-circle protectors designed into the force-sensing screwdriver (section V-C and Fig. 19) are another example. Under large loads, the thin elastic levers deform until the robust protectors touch the casing, limiting additional deflection.

IV. SOFTWARE

This section introduces the open-source software provided together with our 3D printed sensors.

A. OpenSCAD

All sensors presented in this paper were designed using the OpenSCAD programming language and tools [62]. We implemented a set of libraries with 3D models of all required external components to support the design process: proximity- and interrupter-types optical sensors, microcontroller boards, electronic SMD components, nuts, and screws. Using the computational geometry operators built into OpenSCAD (e.g. union, difference, hull, Minkowski), sensors can be placed, and precise cutouts for the sensors can be created in the mechanical structures. Export scripts are provided to split the assembled sensor 3D models into separate parts and to generate the individual STL files for 3D printing.

B. ARDUINO FIRMWARE

The low-cost microcontrollers used in our sensors typically feature only a single on-chip analog-digital converter, combined with an on-chip analog multiplexer to switch between 6...10 analog input pins. The basic software algorithm then consists of a main loop that selects the analog inputs in turn, performs one or more cold reads to ensure voltage stabilization at the converter, then averages over a few (2...4) analog samples to reduce noise. The number of A/D samples taken for averaging is limited both by the speed of the A/D converter and the tradeoff between low latency and reduced sensor noise.

While the microcontrollers are fast enough also to perform channel decoupling and calibration, communication bandwidth is often the limiting consideration, especially with serial communication at low bit rates (e.g. 115200 baud). Therefore, our software just sends the raw sensor data to the host computer, and the task of converting to calibrated output values remains with the PC. Even low-end controllers like the Arduino Pro Mini (Atmel AVR, 8 MHz) can sample and publish eight analog channels at about 200 Hz sample rate.

C. ROS DRIVERS AND UTILITIES

In addition to the Arduino firmware, we also provide open-source ROS drivers and utilities for our sensors, bundled as the *tams_printed_ft* package. Based on the concept of interacting communicating nodes and a standardized hierarchical message format, ROS [63], [64] has established itself as the most popular robot middleware.

Implemented in Python, our sensor ROS drivers convert the raw sensor readings received from the microcontroller into calibrated force and torque data, encapsulated using the ROS *sensor_msgs/Wrench* data type. The drivers also publish the raw sensor values as a float array. As usual, relevant driver parameters can be specified at runtime or in launch files. The sensor drivers work with serial communication as well as with socket communication (e.g. WiFi + UDP).

Sensor calibration data is stored in YAML files and is uploaded to the ROS parameter server before the driver node starts. The calibration files also include channel bias and underload/overload limits in addition to the actual channel-to-force/torque calibration matrices.

One significant advantage of the ROS ecosystem is the interoperability, and many great visualization and debugging tools are available (e.g. *rviz*, *PlotJuggler*). Apart from the sensor drivers and associated launch and configuration files, the *tams_printed_ft* package also provides URDF 3D models of the sensors, using the same STL meshes that were used for printing.

The *radial_gray_scale* tool can generate the special grayscale bitmap images required for force/torque decoupling in our planar reflex-type sensors (Fig. 10). The colored overlay rectangles in the left part of the figure indicate the regions illuminated by the six proximity-type sensors. Three sensors measure plate z -distance (blue) to reconstruct F_z , M_x , and M_y . The three remaining sensors look at grayscale gradients to measure (x, y) plate deflection to reconstruct F_x , F_y , and M_z . Note the shifts and different spread angles of the grayscale ramps to compensate for slight offsets in actual sensor mount positions on the 3D printed specimen. The eight sensor variant (right) demonstrates the combination of four medium-gray areas for z -distance estimation, two areas with sharp black/white transitions for y and two areas with gradual grayscale for x measurements.

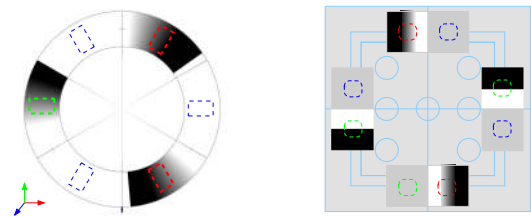


FIGURE 10. Sensor patterns for reflex-type sensors in planar arrangements. (left) Six-sensor (60° spacing) radial grayscale pattern. (right) Eight sensor variant (90° alignment) combining medium-gray areas, two sharp and two soft linear gradients. See the text for details.

D. SENSOR CALIBRATION

While raw sensor data may be suitable for deep learning approaches, most control applications will require sensor calibration. Force sensor calibration is an established field of research, and all common approaches (e.g. known test forces, gravity-based, shape-from-motion) can also be applied to the 3D printed sensors [65]–[68].

The basic method fixes the sensor in a known orientation. Different reference loads are then applied to the sensor (e.g. a number of coins of known weight, Fig. 11), and raw outputs are recorded. Once enough measurements have been taken, a numerical regression is run to estimate the sensor calibration matrix (linear terms) or calibration function (including nonlinear terms). The experiment is repeated with different sensor orientations to apply loads to all sensor axes. As this method can be performed without any additional equipment, it is perhaps the best match for low-cost sensors. However, the process takes a lot of time, and errors easily happen. Our ROS package includes a simple *coins_calibration* program that helps to count, calculates the reference load, and writes a CSV-file for the calibration scripts described below.

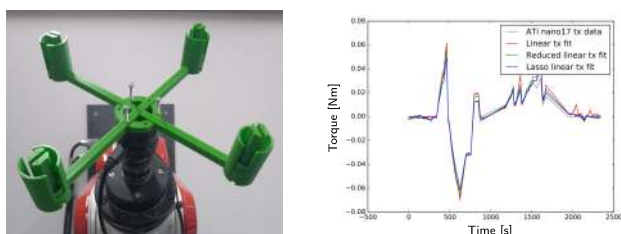


FIGURE 11. Basic sensor calibration with known payloads. (a) The 3D printed jig is filled with a number of coins, and the resulting force and torque are calculated from the known geometry. (b) Example calibration result for $M_x(t)$ [Nm].

If another already calibrated force/torque sensor is available, a much quicker approach can be used (Fig. 12). Both sensors are mounted together, typically aligned along the z -axis and with parallel x - and y -axes. Forces applied to one sensor will then be measured also on the second sensor, while the z -axis offset needs to be considered for applied torques. The wrench measured by the reference sensor is then recorded together with raw data from the target sensor, and numerical regression is run once enough data points have been sampled.

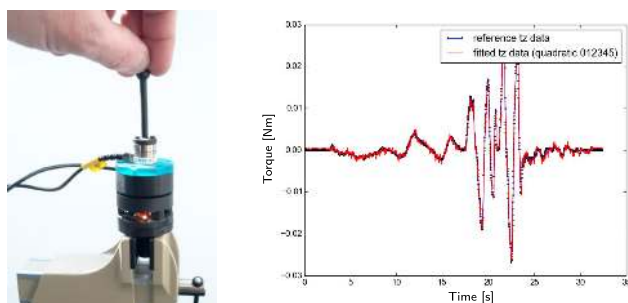


FIGURE 12. Sensor calibration using a second reference sensor. (a) ATI nano17e reference sensor mounted on top of the 3D printed sensor; data is then recorded from both devices. (b) Example results for $M_z(t)$ [Nm].

A third approach uses a fixed sensor payload and measures raw sensor outputs together with an estimate of sensor orientation in space, e.g. using an IMU sensor. Given enough data samples, the payload, as well as the offset of the center of

gravity from the sensor frame and the full calibration matrix, can be recovered [68]. If a robot arm is available, the sensor can be mounted to the arm and sensor output can be measured in different arm poses, with sensor orientation then calculated by forward kinematics of the arm.

Assuming that the raw sensor readings are a continuous function of applied force and torque, we can approximate the true sensor output by a Taylor-series expansion, starting with the constant sensor readings taken from the unloaded sensor, and then adding terms of higher order. For strain-gauge sensors, usually only the linear terms are kept because the mechanical deflections are small (a few μm) and the sensor response is quite linear. The situation is less clear for the optical sensors because of the non-linear sensor response (compare Fig. 2) and the larger beam deflections. As we shall see, at least some of the pure quadratic terms should be included for sensors based on spiral springs (Fig. 15).

In any case, the output wrench $W = (F, M)^T$ combining forces and moments measured in the sensor reference frame can be written as a function of n raw sensor inputs $S = (s_0, s_1, \dots, s_{n-1})^T$ in matrix form,

$$W = \begin{pmatrix} F_x \\ F_y \\ F_z \\ M_x \\ M_y \\ M_z \end{pmatrix} = C + LS + S^T QS + \dots \quad (5)$$

where C is a six-element vector of constant elements, L is a $6 \times n$ matrix of linear calibration coefficients, Q is a $6 \times n \times n$ tensor of quadratic coefficients, and higher-order terms have been suppressed.

To find the calibration coefficients (C, L, Q) from known reference wrenches $W_{\text{ref},i}$ (either known external payloads or wrenches from a reference sensor, usually with six non-null components), one has to solve the minimization problem

$$\min_{C,L,Q} \sum_{i \in \text{Cal}} \left(W_{\text{ref},i} - W_{\text{est},i} \right)^2 + \lambda \cdot \|C, L, Q\| \quad (6)$$

where $W_{\text{est},i}$ is the estimated wrench calculated from equation 5. The first term measures the estimation error (e.g. least-squares error), where the sum is over all samples taken during the calibration experiment, while the second term represents a weighted regularization to ensure good generalization to unseen inputs.

Our ROS software package provides Python scripts based on the NumPy and SciPy libraries [69]–[71] to estimate the least-squares solution using either linear coefficients only, or by combining linear and quadratic coefficients. The resulting calibration result is plotted and written as a YAML file in the format expected by the sensor driver node.

Additionally, either ridge-regression [72] or LASSO [73] are supported by our scripts, where the latter algorithm is preferred, as it tries to enforce sparsity. For lack of space, only

one example analysis is presented in detail, but the results are typical (Fig 13 and 14). The values are the F_x calibration of a six-axis sensor described in section V-F below. This sensor uses eight reflex-type couplers and a printed pattern as shown in (Fig. 10b). Because no mechanical adjustments can be made to the sensor structure, the calibration step has to identify the actual alignment (positions, orientations, distances) of the sensors with respect to the reflective pattern.

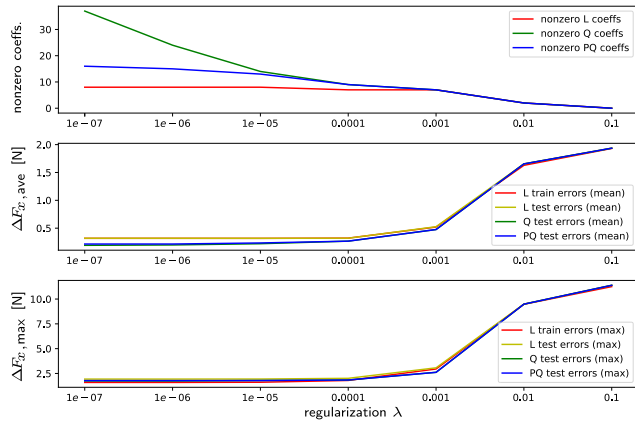


FIGURE 13. Sensor calibration as a function of LASSO regularization. The curves show the calibration of F_x for the sensor described in section V-F. (Top): number of non-zero coefficients for linear terms only, linear and pure quadratic terms, linear and all quadratic terms. (Middle): average absolute test errors of F_x [N] on calibration data set. (Bottom): maximum absolute test errors on the given data set.

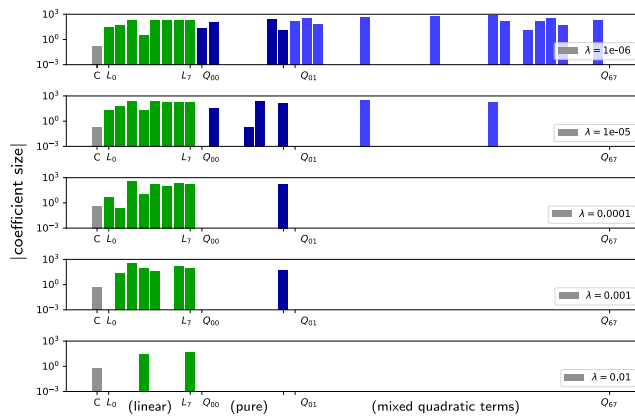


FIGURE 14. Sensor calibration as a function of LASSO regularization. The histograms show the best-fit regression parameters for force F_x using constant (C, gray), linear ($L_0 \dots L_7$, green), pure ($Q_{00}, Q_{11}, \dots, Q_{77}$, blue) and mixed quadratic (Q_{01}, \dots, Q_{67} , light blue) terms for different values of λ . Note overfitting with many non-zero terms for small λ (top) and underfitting for large λ (bottom). LASSO keeps the essential quadratic terms, here Q_{77} .

The example calibration dataset includes 12350 raw data samples, of which 10% were used for regression, while the remaining 90% were used for testing. Three different configurations are presented, L: using linear regression with up to 9 parameters (1 bias C and 8 coefficients $L_0 \dots L_7$); PQ: linear and diagonal pure quadratic terms (1 bias, 8 linear,

8 pure quadratic, $Q_{00}, Q_{11}, \dots, Q_{77}$); and Q: fully quadratic (all of PQ, plus 28 mixed quadratic terms Q_{01}, \dots, Q_{67}).

Here, the pure quadratic terms are tested separately, because they represent nonlinearities of a single sensor, e.g. a reflex-type sensor operated in region-III of its characteristic curve (compare Fig. 2). As the mixed quadratic terms are symmetric, pairs of redundant coefficients like $S_0 Q_{01} S_1$ and $S_1 Q_{10} S_0$ are combined, and only an upper triangular matrix is calculated to improve convergence and performance.

As expected, the number of active (nonzero) parameters decreases with increasing levels of LASSO regularization λ , but the effect on the quality of the regression is initially small. Overall, including quadratic terms improves the mean output errors (Fig. 13 middle, Fig. 15), but does not significantly reduce the maximum errors (Fig. 13 bottom). With increasing values of LASSO regularization λ , only the essential coefficients remain non-zero (Fig. 14).

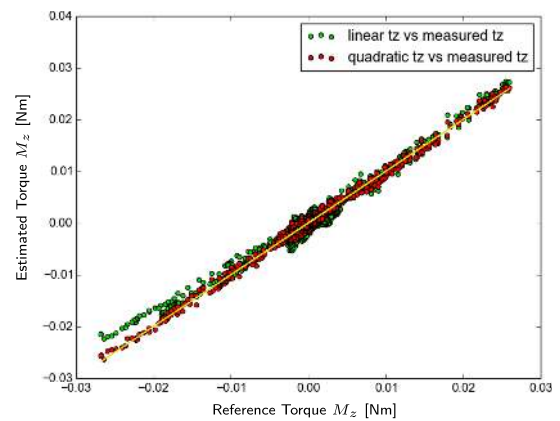


FIGURE 15. Comparison of linear (green) and quadratic (red) calibration of torque M_z in a sensor with spiral spring and six fork-type sensors. The non-linear behavior of the spring is compensated well by including a few quadratic coefficients.

In any case, it is required to check for sensor overload and to remove such data points from further processing, as least-squares regression is not robust to outliers (a single large squared error can dominate smaller errors from many valid data points). If outliers are expected, e.g. due to human errors in dataset labeling, the Huber loss [74] is worth testing:

$$\min_{\omega, \sigma} \sum_{i=1}^n \left(\sigma + H_{\epsilon} \left(\frac{W_{est,i} - W_{ref,i}}{\sigma} \right) \sigma \right) + \alpha \|\omega\|_2^2 \quad (7)$$

$$H_{\epsilon}(z) = \begin{cases} z^2 & \text{if } |z| < \epsilon, \\ 2\epsilon|z| - \epsilon^2 & \text{otherwise} \end{cases} \quad (8)$$

Here, small errors are still weighted quadratically, but outliers are only weighted linearly, greatly reducing their impact. Given a regularization parameter α , the algorithm optimizes for the parameter σ and the calibration vector $\omega = (C, L)$. Huber loss is supported in SciPy and our scripts, and optimization takes only slightly longer than the standard least-squares approximation. Overall, using Huber loss is preferred if outliers are hard to remove, while LASSO results in more

robust estimations than standard least-squares. Useful values for the regularization parameters (λ , α) depend on the sensor in question and can be checked with cross-validation.

V. PROTOTYPES

This section introduces a collection of prototype designs built and tested in our lab for different applications, ranging from basic 1-DOF force sensors to different variants of fully-decoupled six-axis force/torque sensors. Refer to Table 1 for an overview with key properties including application, size, payload, sensor type, microcontroller, and price. Each prototype also demonstrates a specific design problem and our proposed solution, as well as the usage of different low-cost microcontrollers. We also describe a few lessons learned, hinting at design ideas that did not work.

A. HUMANOID FOOT SENSOR

This sensor, originally described in [75], was designed to measure forces and to estimate center-of-pressure for the humanoid robots of the Hamburg University RoboCup team (Hamburg Bitbots). This sensor illustrates the theme of this paper in its pure form:

- building a custom force sensor for the task at hand,
- 3D printed deflecting beam, one proximity sensor,
- fully integrated into 3D printed structure (robot foot).

The chosen beam dimensions (length of 5 cm) result in a nominal payload of 50 N, matched to the size and weight of the robot (Fig. 16). Each foot is equipped with four of these sensors, with the deflecting levers pointing to the corners of the foot. All four sensors of each foot are connected to one microcontroller (Teensy 3.0), so that total force and center-of-pressure can also be estimated locally.

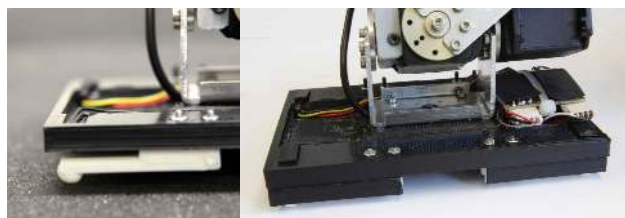


FIGURE 16. Foot force sensor of the Hamburg Bitbots Robocup team. (a) Basic 1-DOF force sensor, combining a deflecting lever and a single reflex-type optical sensor. (b) View of the whole 3D printed robot foot with four sensors, optical shielding, and microcontroller on the right.

The sensor worked well and was used during tournaments. Beam deflection under full load was about 1.5 mm, providing significant impact dampening during walking, but also introducing series-elastic behavior complicating static balancing. The original 3D printed beam lacked proper mechanical end-stops as overload protection and would occasionally break.

B. FRICTION-FORCE SENSOR FOR OBJECT PUSHING

Object pushing on planar surfaces is one of the simplest manipulation tasks, yet remains an unsolved research topic, because pushing is inherently unstable and the actual object

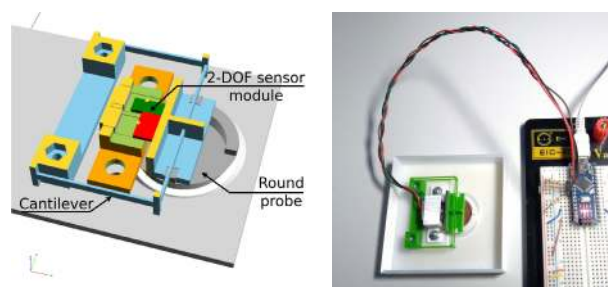


FIGURE 17. 2-DOF friction-force sensor for object pushing. (a) CAD model. The round probe (dark gray) is mounted on a thin parallel cantilever (blue) and ballasted with a known weight (5-cent coins). Probe deflection in (x , y) is measured by a 2-DOF sensor module. Red and green fins intersect light beams (yellow) as introduced in Fig. 5. (b) Prototype test.

motion depends on the combination of the applied force and the unknown friction forces between object and surface.

The simple sensor module shown in Fig. 17 is designed to measure sliding forces in robot pushing experiments, and will be mounted into several test objects of different sizes, shapes, and weight distribution. It consists of a small circular probe with sloped sides, ballasted with a known weight that touches and slides across the table surface. The probe is attached to the main object body via double thin cantilevers that allow parallel probe deflection along the x -, y -, and z -axes, while probe rotation is considerably constrained. When the main body is pushed, the probe deflects due to friction, and this deflection in turn is measured with one 2-DOF sensor module presented in section III-D above. Key points of the sensor:

- 2-DOF force sensor for a specific task,
- modular construction, here the 2-DOF sensor module,
- interchangeable spring elements, very low stiffness,
- efficient use of 3D printing (free-hanging bridges).

Given the crude approximations of the empirical Coulomb friction model, an adequate sensor calibration can be calculated from the known normal force of the probe (total mass about 9 grams) and the friction coefficient for the material pair (e.g., plastic probe on a wooden table).

Example data recorded during a sensor test is shown in Fig. 18, where the different phases of the motion (up/down, left/right, circles) are clearly visible, as are the transitions between static and sliding friction. We are currently working on combining the sensor data with visual tracking for autonomous object pushing using deep networks.

C. INSTRUMENTED SCREWDRIVER

Learning from human demonstration is an essential part of our research into dexterous robot manipulation [76]. The instrumented screwdriver introduced in this section is designed for experiments on human tool use (Fig. 19 and 20):

- 4-axis tool torque sensor (F_z , M_x , M_y , M_z),
- grasp handle measures applied finger forces ($F_z \times 12$),
- housing and elastic elements all 3D printed,
- Arduino Nano 33 IOT with WiFi chip and 6-axis IMU,
- battery-powered, wireless operation.

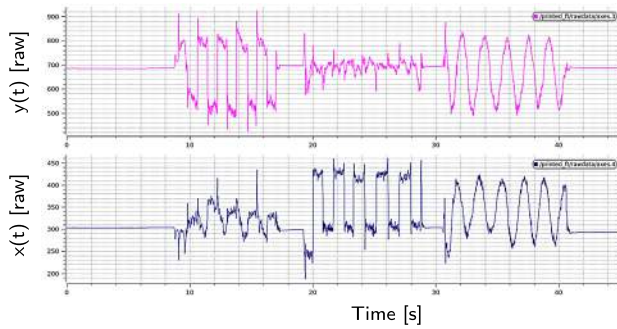


FIGURE 18. Example raw output signals from the friction-force sensor while sliding on a table, blue: $x(t)$, magenta: $y(t)$. Up/down motion followed by left/right motion followed by circular motion, each repeated five times.

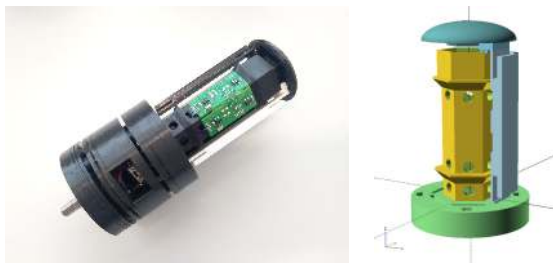


FIGURE 19. Force-sensing screwdriver for recording human manipulation motions. (a) Photo of the partly assembled object. (b) CAD rendering of the grasp handle with central column and elastic (deflecting) outer grasp faces.

The prototype comprises a total of 17 optical sensors, divided into two functional groups. The *torque-sensing tool mount* consists of a 3D printed standard 1/4 inch bit holder that takes any common screw bit. Compared to common metal-based tools, the maximum torque that can be applied to the screw bit is much lower, but still sufficient for light screwing tasks. The thin elastic levers are protected by robust overload end stops. The bottom face of the screw-bit holder features a printed grayscale pattern atop a set of five reflex-type optical sensors in a planar cross-type arrangement, measuring normal force and moments applied to the tool.

The *hexagonal grasp handle* consists of six independent cantilevers with fixed supports on the upper and lower ends. Two reflex-type sensors are mounted on the inner core of the handle below each cantilever (a total of 6×2 sensors). The grasp faces deflect under finger contacts, measuring the total force applied to the cantilever and allowing for a rough reconstruction of the contact location on the grasp handle.

D. SMALL SIX-AXIS FORCE/TORQUE SENSORS

This section describes a six-axis force-torque sensor based on a planar configuration of six photointerrupters. Originally intended as a replacement for the ATi nano17 [77] strain-gauge sensor in robot object-shape detection and contour-following tasks, the goal was to detect tool-tip forces as low as 0.02 N, to avoid pushing the touched objects. Key properties of the design can be summarized as follows:



FIGURE 20. (a) CAD model of the tool part with 1/4 inch bit holder and five reflex-type sensors. (b) Bit holder elastic element with Pozidriv bit; note thin double levers and quarter-circle overload end stops.

- six-axis F/T sensor, $(F_x, F_y, F_z, M_x, M_y, M_z)$,
- compact size ($d = 42$ mm, $h = 35$ mm, $m = 150$ g),
- integrated microcontroller, USB or serial interface,
- exchangeable “hats” with different stiffness,
- prone to torsional vibrations under high inertial loads.

To realize a densely packed design, we selected a planar hexagonal sensor layout around a central column combined with construction from three main parts (Fig. 21). The top part or *tool adapter* is formed by an outer ring with mounting screws and a spiral spring as the elastic element. The outer ring also carries six fins, with alternating shorter fins that reach into three of the photointerrupters from above to measure z -deflection, and longer fins reaching sideways into the remaining photointerrupters to detect (x, y) deflections. A single M4 screw is used to fix the upper elements to the central column, with key and slot notches on both parts to ensure correct and precise alignment.

The middle *sensor carrier* component consists of a single 3D printed part with six cutouts for the used TCST 1103 [51] sensors, the central bore and hex-nut cutout for fixing the upper ring, and another set of six outer bores. The outer screws mount to the base plate and are also used as the robot-side attachment.

The *base plate* houses the electronics. Due to the length of the selected microcontroller (Teensy 3.2), only four of the outer six hexagonal positions remain available for the screws that connect the base and middle parts.

All three main parts are designed with 3D printability in mind, and can be printed on FFF-printers without support structures. We also built prototypes using an SLA printer (Formlabs Form 2) with much better nominal geometric accuracy. Unfortunately, the SLA-printed spiral springs were not usable, as the tested resin materials either showed unexpected mechanical hysteresis or significant creep. However, a material mix with SLA for the sensor carrier part and FFF-printed PLA for the spiral spring works fine.

Unfortunately, the mechanical dimensions of the photointerrupter itself are only specified to a tolerance of ± 0.2 mm by the vendor; this includes the alignment of the transmitter LED and the phototransistor inside the sensor housing, which might shift a bit during soldering. As this range also corresponds to the measured deflection for the on-off transition of

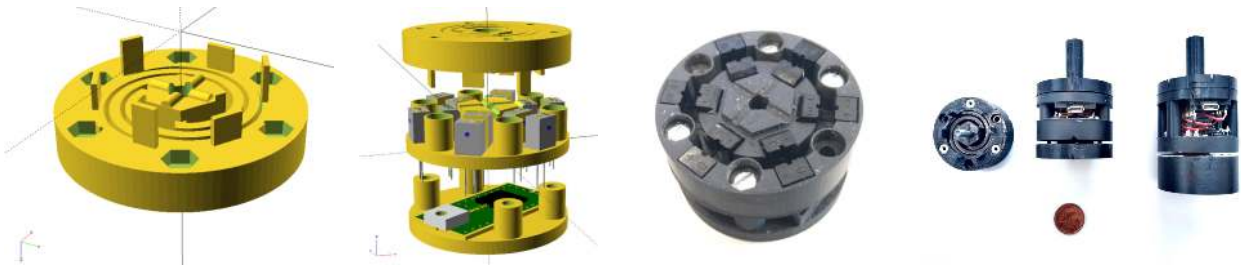


FIGURE 21. Six-axis fork-type F/T Sensor. (a) OpenSCAD rendering of the elastic member with alternating short and long optical fins. (b) Three part construction with elastic member (top), middle plate with six photointerrupters spaced at 60 degrees, and bottom housing for wiring and Teensy 3.2 microcontroller. (c) Top view of the SLA-printed middle plate with mounted photointerrupters. (d) Exchangeable tool plates (“hats”), showing a thin tool plate for the fork-type sensor; side view of the thin tool plate mounted; and side view of a thicker and stronger tool plate mounted on the reflex-type sensor.



FIGURE 22. Six-axis F/T sensor using eight fork-type interrupters and adjustable fins; $d = 104$ mm, $F_x, F_y, F_z = 20$ N. (a) OpenSCAD rendering with the key parts (top to bottom): four 2-DOF sensor modules and microcontroller, fixed upper ring with sensor housings, four quarter-circle sheets with adjustable 45-degree fins, moving tool-mounting ring with spiral spring. (b) Upper ring with sensor-modules and microcontroller. (c) Base ring with spiral spring and adjustable fins installed. (d) Close-up view of two adjusted fins on the assembled sensor.

the photointerrupter (compare Fig. 2), the precise mechanical alignment of six sensors and six fins is a challenge.

Our solution is a straightforward manual approach. The sensor carrier is built and wired first so that sensor signals can be sampled. The tool plate is printed with slightly oversized fins, so that initially all photointerrupters are blocked. The fins are then filed manually, very carefully, until the unloaded sensor plate shades half the light beams. Wriggling the tool plate indicates how much extra material is still there. The process requires a bit of patience, as filing away too much material will leave fins too short or too thin, requiring to start over with a new part.

An interesting feature of the design is the modular construction, which allows us to exchange the elastic element literally at the turn of a single screw. Only the dimensions of the sensor fins and the inner mounting flange are fixed; other parameters like overall thickness and the dimension of the spiral spring can be changed at will. This way, several “hats” with different stiffness and maximum force limits can be prepared and exchanged quickly as needed (Fig. 21d).

For comparison, we also built a very similar design based on reflex-type sensors [50] (sensor layout as in Fig. 6c). The sensor shares the same outer dimensions, central mounting column concept, and the planar hexagonal sensor layout. Instead of the fins used on the fork-type sensor, suitable radial grayscale patterns are then glued to the bottom of the tool plate. While sensitivity to z -axis deflection (F_z, M_x, M_y) is

given by the reflex-type sensor characteristics, the effective range for z -axis torsion and (x, y) -plane motions (F_x, F_y, M_z) can be selected by printing grayscale gradients with different slopes (Fig. 10a).

E. ADJUSTABLE SIX-AXIS F/T SENSOR

The sensor presented in this section uses adjustable fins, which greatly simplifies first commissioning and later recalibration. The basic concept again uses photointerrupters and a spiral spring, and a construction of two main parts designed for 3D printability, but several changes demonstrate the flexibility and scalability of our approach (Fig. 22):

- larger physical size ($d = 104$ mm, $h = 42$ mm),
- spiral spring with much longer and thicker arms, resulting in much smaller relative deflection $\Delta l/l$,
- hollow core as cable/tube pass-through,
- planar redundant sensor configuration (8 sensors),
- using four 2-DOF sensor modules,
- fins on flexible plates, adjustable by grub screws.

The sensor setup suggested here uses four of our 2-DOF sensor modules on the fixed (robot side) carrier plate. The photointerrupters in each module are mated to two separate triangular fins attached to the moving (tool side) part, with their active edge angled about 45 degrees with respect to the carrier plate. The fins are part of thin intermediate sheets of plastic attached to the actual tool plate and can be displaced

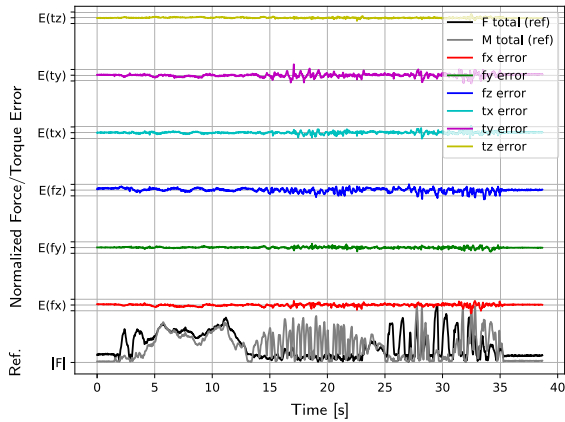


FIGURE 23. Accuracy of the adjustable F/T sensor using linear calibration. The curves show the errors of (F_x, F_y, F_z) and (M_x, M_y, M_z) vs. time, normalized to the maximum forces (black) and torques (gray) from the reference sensor. Scale: (1 div = full-scale, intermediate grid lines = 10% full-scale).

slightly by grub screws inserted into the tool plate. By design, the fins are a bit too short to obstruct the light beams. Once the sensor is assembled, all fins are then individually trimmed upwards into the zero position of their photointerrupter.

Using 45-degree fins results in a fully symmetric mechanical design, but the axis-decoupling is no longer achieved due to the structure alone (compare the combined stacked 0/90-degree fins described above, Fig. 5). However, full axis-decoupling is recovered after sensor calibration.

Typical calibration λ results are shown in Fig. 23 (normalized accuracy over time) and Fig. 24 (accuracy histogram), with reference data provided by an external industrial six-axis F/T sensor (Sunrise Instruments, M3207). The slight skew in F_x and M_y originates from the experiment setup, with both sensors aligned and stacked along the z -axis, but x instead of z pointing upwards. In this situation, the own weight of the sensor introduces a small offset that was not modelled. As can be seen from the histograms, most errors are well below 2% of full range, but a few outliers go up to 10%.

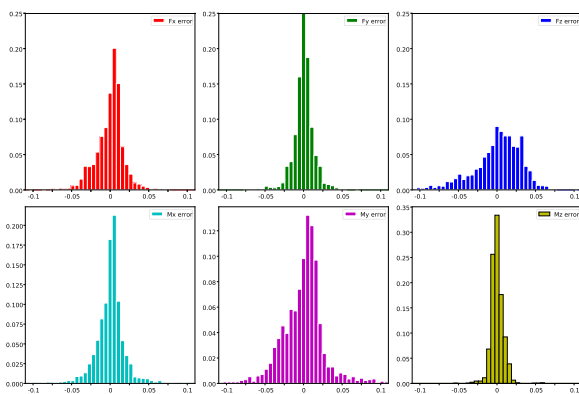


FIGURE 24. Error histograms of the adjustable F/T sensor after linear calibration with LASSO $\lambda = 10^{-6}$. The histograms show the errors of (F_x, F_y, F_z) (top row) and (M_x, M_y, M_z) (bottom row) normalized to the maximum forces and torques from the reference sensor. Note slight skew in F_x and M_y . See the text for details.

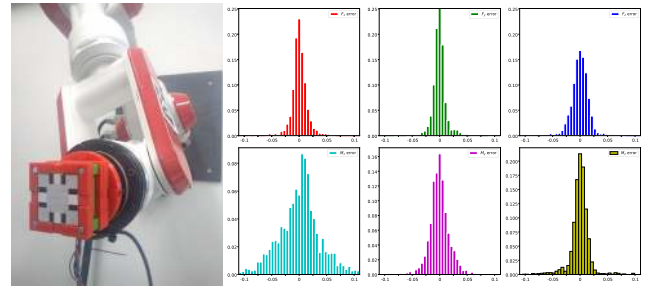


FIGURE 25. Six-axis F/T sensor mounted on a PA10-6C robot, $d = 56$ mm, $h = 36$ mm, $F_x = F_y = F_z = 11$ N. This sensor has eight reflex-type sensors in a planar layout with a printed reflecting grayscale pattern and uses the custom elastic element presented above (compare Fig. 7 and 10b). Error histogram after calibration using quadratic terms and LASSO $\lambda = 10^{-5}$, (top row): (F_x, F_y, F_z) , (bottom row): (M_x, M_y, M_z) .

A detailed analysis shows that the larger errors can be traced back to two reasons, namely timing and near-overload. First, axis-decoupling is not perfect, and somewhat increased errors are expected for channels reading small values while other channels are fully loaded (e.g. M_y error in Fig. 23 during $t = 15 \dots 22$ s). Second, if the load applied to the sensor changes quickly, the output values will highly depend on the exact sampling times. As the Arduino Nano microcontroller used in the prototype has only a single A/D converter, the eight photointerrupters are read in sequence, and some error is expected in high-gradient situations. A faster microcontroller or A/D converter would alleviate this problem.

The payload of the sensor is again defined by the spiral spring, and can be selected by adjusting the dimensions of the spring. As the sensors and electronics are all on the (fixed) base plate, it is possible to quickly change the sensor response simply by exchanging the tool plate with the spring, followed by a quick adjustment of the fins.

Apart from the linear deflection along the (x, y, z) -axes, tilt must also be considered carefully when designing a sensor, especially when combined with a large (long) end effector. Considering the maximum sideways deflection (0.2 mm) of the fins for saturation of the photointerrupters and the radial distance between sensors (about 95 mm), the maximum pitch/yaw deflection angle for this sensor is

$$\phi, \psi \leq \arctan(0.2/(95/2)) \approx 0.24^\circ. \quad (9)$$

For comparison, effective sensor distance between photointerrupters is just 36 mm for the smaller sensors presented in the previous subsection; resulting in a larger maximum angular deflection of up to 0.7° .

F. PLANAR REFLEX-TYPE F/T SENSOR

If larger deflections are wanted than are possible with fork-type interrupters, reflex-type optocouplers operated in their far distance region (region-III in Fig. 2) provide the obvious solution. As the operating distance between the sensors and the reflecting surface can be in the range of a few millimeters, slight manufacturing differences are tolerated:

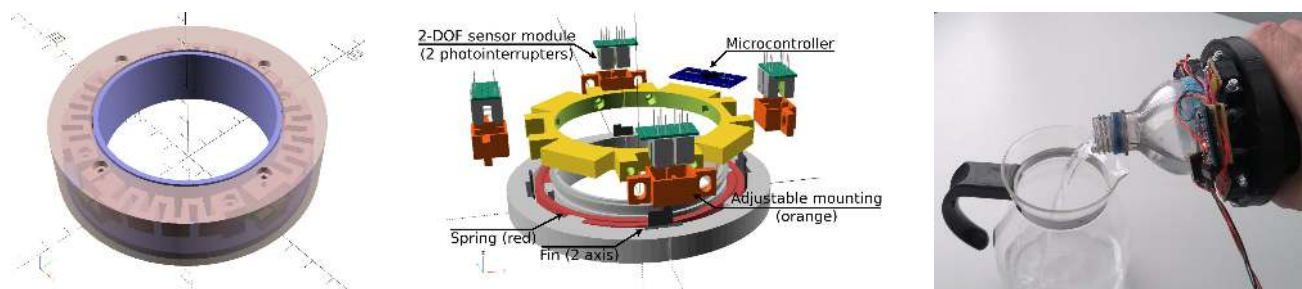


FIGURE 26. Ring-type F/T sensor for measuring forces during liquid-pouring tasks. (a) Original (unsuccessful) design with outer grasp part (pink), inner bottle carrier (blue), zigzag elastic springs. (b) Redesigned sensor with spiral spring, adjustable 2-DOF sensor modules, and Arduino microcontroller. (c) Prototype.

- planar reflex-type sensor layout,
- custom black/white or grayscale reflective pattern,
- no mechanical z-adjustment needed,
- large (x, y)-deflections possible (≥ 5 mm).

Fig. 25 shows a six-axis F/T prototype built around the elastic beam element described above (compare Fig. 7). A planar set of eight reflex-type optocouplers is mounted above the fixed rectangular core of the beam structure, measuring reflection from the moving laser-printed grayscale pattern (Fig. 10b) fixed to the moving part. (The active pattern is of course on the inside of the cover, but our prototype features two different patterns on both sides of the pattern plate.)

Given the beam dimensions (compare table 2), the measured useful force range after calibration was indeed 11 N for the three (F_x, F_y, F_z) axes, and about (0.5, 0.25, 0.4) Nm for (M_x, M_y, M_z). As expected, the force limits are about the same for all axes, but M_y has a lower maximum range than M_x and M_z due to the smaller distance and (unwanted) torsion of the x-levers (Fig. 7). Force-/torque decoupling works as expected after calibration, but the noise level is somewhat higher compared to the adjustable fork-type sensor presented above, as a smaller fraction of the total voltage-swing of the analog-digital converter is actually used.

Note that the sensor response to (x, y)-deflections and z-rotations (roll) can be adjusted by printing steeper or softer grayscale gradients; very compliant sensors can be built if needed. Of course, mechanically, other elastic structures including spiral springs can be combined with reflex-type optical sensors.

G. RING-TYPE F/T SENSOR

Another example of a custom shaped sensor, the *bottle-ft* sensor shown in Fig. 26 is designed to track and record human motions during liquid pouring tasks, with the human grasping pose and motions as natural as possible. We selected a ring-type sensor concept, where the inner hollow part provides a snug fit with the bottle and moves with respect to the outer ring and grasping handle. As the diameter of the outer ring is in the range of typical bottles, normal hand poses and arm motions can be used (Fig. 26):

- force/torque range optimized for 0.5 l water bottles,

- custom ring shape (inner diameter 72 mm),
- cylindrical handle for natural grasp postures.

Unfortunately, our first design proved a failure (Fig. 26a). It featured a clean outer ring for grasping, connected via four separate roughly quarter-circle shaped springs to the bottom/inner part of the sensor carrying the bottle. Four 2-DOF sensor modules (fork-type) were mounted on the bottom ring and occluded by fins on the springs. While the SLA-printed parts had low mechanical tolerances, the spring mounting concept with single screws to the outer and inner rings was not precise enough, as fastening one screw would slightly distort either ring and introduce a new offset to the fork-type sensors. The springs were another source of trouble, as their total angle was below a quarter-circle, resulting in quite different stiffness for (x, y)-deflections, adding distortions to both rings, and wearing out the mountings.

The redesigned prototype (Fig. 26b) therefore again uses a spiral spring, with inner and outer moving rings 3D printed as a single part. The 2-DOF sensor modules are reused, but these are now mounted in separate sensor carriers with long holes that can be adjusted in two dimensions with respect to the fins on the outer ring. For the pouring experiments, a separate 3D printed grasping cylinder is glued to the outer ring, with enough spacing to the bottle to not obstruct tilt.

VI. CONCLUSION AND FUTURE WORK

In this paper, we introduced a design approach for low-cost 3D printed force/torque sensors based on optical proximity or photointerrupter sensors. While the basic design principles are widely known, creating functional multi-axis sensors can be quite tricky, as precise alignment of all components and careful consideration of 3D printing quirks and defects are needed. We presented a set of workable example designs, ranging from a simple 1-DOF force sensor to fully decoupled six-axis F/T sensors of different shapes. We also discussed electronics and sensor calibration. OpenSCAD designs, Arduino firmware, and ROS drivers are open-source:

github.com/TAMS-Group/tams_printed_ft

To improve the sensors, we currently focus on improved sensor designs based on the recent digital proximity sensor

chips, with better accuracy and ambient light suppression due to the built-in amplifiers.

We are also working on a hybrid manufacturing approach, where the optical sensors and electronics components are automatically inserted and connected during the 3D printing process. We use a modified printer with an integrated pick and place system and a dispenser for conductive silver paste to print wires. Printing both the structural and electronic parts of custom sensors would significantly facilitate the assembling step.

REFERENCES

- [1] M. R. Cutkosky, R. D. Howe, and W. R. Provancher, "Force and tactile sensors," in *Springer Handbook of Robotics*. Berlin, Germany: Springer-Verlag, 2008, pp. 455–476. [Online]. Available: <https://link.springer.com/referencework/10.1007%2F978-3-540-30301-5>, doi: 10.1007/978-3-540-30301-5.
- [2] D. M. Perry, "Multi-axis force and torque sensing," *Sensor Rev.*, vol. 17, no. 2, pp. 117–120, Jun. 1997.
- [3] J. O. Templeman, B. B. Sheil, and T. Sun, "Multi-axis force sensors: A state-of-the-art review," *Sens. Actuators A, Phys.*, vol. 304, Apr. 2020, Art. no. 111772.
- [4] J. T. Muth, D. M. Vogt, R. L. Truby, Y. Mengüç, D. B. Kolesky, R. J. Wood, and J. A. Lewis, "Embedded 3D printing of strain sensors within highly stretchable elastomers," *Adv. Mater.*, vol. 26, no. 36, pp. 6307–6312, Sep. 2014.
- [5] A. Matute, L. Paredes-Madrid, E. Gutierrez, and C. A. P. Vargas, "Characterization of drift and hysteresis errors in force sensing resistors considering their piezocapacitive effect," in *Proc. IEEE SENSORS*, Oct. 2017, pp. 1–3.
- [6] M. Shimojo, T. Araki, A. Ming, and M. Ishikawa, "A ZMP sensor for a biped robot," in *Proc. IEEE Int. Conf. Robot. Autom.*, May 2006, pp. 1200–1205.
- [7] S. J. Leigh, R. J. Bradley, C. P. Purssell, D. R. Billson, and D. A. Hutchins, "A simple, low-cost conductive composite material for 3D printing of electronic sensors," *PLoS ONE*, vol. 7, no. 11, Nov. 2012, Art. no. e49365.
- [8] S. C. Gomez, M. Vona, and D. Kanoulas, "A three-toe biped foot with Hall-effect sensing," in *Proc. IEEE/RSJ Int. Conf. Intell. Robots Syst. (IROS)*, Sep. 2015, pp. 360–365.
- [9] R. Bekhti, V. Duchaine, and P. Cardou, "Miniature capacitive three-axis force sensor," in *Proc. IEEE/RSJ Int. Conf. Intell. Robots Syst.*, Sep. 2014, pp. 3939–3946.
- [10] Y.-L. Park, K. Chau, R. J. Black, and M. R. Cutkosky, "Force sensing robot fingers using embedded fiber Bragg grating sensors and shape deposition manufacturing," in *Proc. IEEE Int. Conf. Robot. Autom.*, Apr. 2007, pp. 1510–1516.
- [11] K. Weiß and H. Worn, "The working principle of resistive tactile sensor cells," in *Proc. IEEE Int. Conf. Mechatron. Autom.*, vol. 1, Jul. 2005, pp. 471–476.
- [12] M.-C. Chou, J.-Y. Chang, C. Yang, G.-T. Lin, T.-H. Kao, and M.-C. Huang, "A novel design and fabrication of tactile sensor for humanoid robot finger," in *Proc. IEEE/ASME Int. Conf. Adv. Intell. Mechatron. (AIM)*, Jul. 2018, pp. 444–447.
- [13] R. S. Dahiya, G. Metta, M. Valle, and G. Sandini, "Tactile sensing—From humans to humanoids," *IEEE Trans. Robot.*, vol. 26, no. 1, pp. 1–20, Feb. 2010.
- [14] H. Yousef, M. Boukallel, and K. Althoefer, "Tactile sensing for dexterous in-hand manipulation in robotics—A review," *Sens. Actuators A, Phys.*, vol. 167, no. 2, pp. 171–187, Jun. 2011.
- [15] Z. Kappassov, J.-A. Corrales, and V. Perdereau, "Tactile sensing in dexterous robot hands—Review," *Robot. Auto. Syst.*, vol. 74, pp. 195–220, Dec. 2015.
- [16] M. Kaneko, "A new design of six-axis force sensors," in *Proc. IEEE Int. Conf. Robot. Autom. (ICRA)*, vol. 1, May 1993, pp. 961–967.
- [17] A. Bicchi, "A criterion for optimal design of multi-axis force sensors," *Robot. Auto. Syst.*, vol. 10, no. 4, pp. 269–286, Jan. 1992.
- [18] M. M. Svinin and M. Uchiyama, "Optimal geometric structures of force/torque sensors," *Int. J. Robot. Res.*, vol. 14, no. 6, pp. 560–573, Dec. 1995.
- [19] A. Bicchi, A. Caiti, and D. Prattichizzo, "Optimal design of dynamic multi-axis force/torque sensor," in *Proc. 38th IEEE Conf. Decis. Control*, vol. 3, Dec. 1999, pp. 2981–2986.
- [20] A. Parmiggiani, M. Maggiali, L. Natale, F. Nori, A. Schmitz, N. Tsagarakis, J. Santos-Victor, F. Becchi, G. Sandini, and G. Metta, "The design of the icub humanoid robot," *Int. J. Humanoid Robot.*, vol. 9, no. 4, Dec. 2012, Art. no. 1250027.
- [21] M.-K. Kang, S. Lee, and J.-H. Kim, "Shape optimization of a mechanically decoupled six-axis force/torque sensor," *Sens. Actuators A, Phys.*, vol. 209, pp. 41–51, Mar. 2014.
- [22] D. Okumura, S. Sakaino, and T. Tsuji, "Development of a multistage six-axis force sensor with a high dynamic range," in *Proc. IEEE 26th Int. Symp. Ind. Electron. (ISIE)*, Jun. 2017, pp. 1386–1391.
- [23] D. Okumura, S. Sakaino, and T. Tsuji, "High dynamic range sensing by a multistage six-axis force sensor with stopper mechanism," in *Proc. IEEE Int. Conf. Robot. Autom. (ICRA)*, May 2018, pp. 4065–4070.
- [24] D. Okumura, S. Sakaino, and T. Tsuji, "Miniaturization of multistage high dynamic range six-axis force sensor composed of resin material," in *Proc. Int. Conf. Robot. Autom. (ICRA)*, May 2019, pp. 4297–4302.
- [25] K.-J. Xu and C. Li, "Dynamic decoupling and compensating methods of multi-axis force sensors," *IEEE Trans. Instrum. Meas.*, vol. 49, no. 5, pp. 935–941, Oct. 2000.
- [26] S. Hirose and K. Yoneda, "Development of optical six-axis force sensor and its signal calibration considering nonlinear interference," in *Proc. IEEE Int. Conf. Robot. Autom. (ICRA)*, vol. 1, May 1990, pp. 46–53.
- [27] D. Tsetserukou, R. Tadakuma, H. Kajimoto, and S. Tachi, "Optical torque sensors for implementation of local impedance control of the arm of humanoid robot," in *Proc. IEEE Int. Conf. Robot. Autom. (ICRA)*, May 2006, pp. 1674–1679.
- [28] S. H. Jeong, H. J. Lee, K.-R. Kim, and K.-S. Kim, "Design of a miniature force sensor based on photointerrupter for robotic hand," *Sens. Actuators A, Phys.*, vol. 269, pp. 444–453, Jan. 2018.
- [29] Y. Liu, T. Tian, J. Chen, F. Wang, and D. Zhang, "A highly reliable embedded optical torque sensor based on flexure spring," *Appl. Bionics Biomech.*, vol. 2018, pp. 1176–2322, Apr. 2018.
- [30] J.-C. Kim, K.-S. Kim, and S. Kim, "Note: A compact three-axis optical force/torque sensor using photo-interrupters," *Rev. Sci. Instrum.*, vol. 84, no. 12, Dec. 2013, Art. no. 126109.
- [31] M. Ohka, Y. Mitsuya, Y. Matsunaga, and S. Takeuchi, "Sensing characteristics of an optical three-axis tactile sensor under combined loading," *Robotica*, vol. 22, no. 2, pp. 213–221, 2004.
- [32] M. Ohka, H. Kobayashi, J. Takata, and Y. Mitsuya, "Sensing precision of an optical three-axis tactile sensor for a robotic finger," in *Proc. 15th IEEE Int. Symp. Robot Hum. Interact. Commun. (ROMAN)*, Sep. 2006, pp. 214–219.
- [33] A. Tar and G. Cserey, "Development of a low cost 3D optical compliant tactile force sensor," in *Proc. IEEE/ASME Int. Conf. Adv. Intell. Mechatronics (AIM)*, Jul. 2011, pp. 236–240.
- [34] M. Costanzo, G. De Maria, C. Natale, and S. Pirozzi, "Design and calibration of a force/tactile sensor for dexterous manipulation," *Sensors*, vol. 19, no. 4, p. 966, Feb. 2019.
- [35] J. Díez, J. Catalán, A. Blanco, J. García-Perez, F. Badesa, and N. Gacía-Aracil, "Customizable optical force sensor for fast prototyping and cost-effective applications," *Sensors*, vol. 18, no. 2, p. 493, Feb. 2018.
- [36] G. Palli, L. Moriello, U. Scarcia, and C. Melchiorri, "Development of an optoelectronic 6-axis force/torque sensor for robotic applications," *Sens. Actuators A, Phys.*, vol. 220, pp. 333–346, Dec. 2014.
- [37] A. P. Boreasi et al., *Advanced Mechanics of Materials*, vol. 6. New York, NY, USA: Wiley, 1985.
- [38] J. M. Gere and B. J. Goodino, *Mechanics of Materials*, 8th ed. Boston, MA, USA: Cengage Learning, 2012.
- [39] C. Ziemian, M. Sharma, and S. Ziemian, "Anisotropic mechanical properties of ABS parts fabricated by fused deposition modelling," in *Mechanical Engineering*, vol. 23, 2012, ch. 7, pp. 159–180. [Online]. Available: <https://www.intechopen.com/books/mechanical-engineering/anisotropic-mechanical-properties-of-abs-parts-fabricated-by-fused-deposition-modeling>
- [40] T. Letcher and M. Waytashek, "Material property testing of 3D-printed specimen in PLA on an entry-level 3D printer," in *Proc. ASME Int. Eng. Congr. Expo.*, 2014, pp. 1–8.
- [41] B. M. Tymrak, M. Kreiger, and J. M. Pearce, "Mechanical properties of components fabricated with open-source 3-D printers under realistic environmental conditions," *Mater. Des.*, vol. 58, pp. 242–246, Jun. 2014.
- [42] A. Boschetto and L. Bottini, "Accuracy prediction in fused deposition modelling," *Int. J. Adv. Manuf. Technol.*, vol. 73, nos. 5–8, pp. 913–928, Jul. 2014.
- [43] S. B. Kesner and R. D. Howe, "Design principles for rapid prototyping force sensors using 3-D printing," *IEEE/ASME Trans. Mechatron.*, vol. 16, no. 5, pp. 866–870, Oct. 2011.

- [44] A. Taghipour, A. N. Cheema, X. Gu, and F. Janabi-Sharifi, "Temperature independent triaxial force and torque sensor for minimally invasive interventions," *IEEE/ASME Trans. Mechatronics*, vol. 25, no. 1, pp. 449–459, Feb. 2020.
- [45] G. Palli and S. Pirozzi, "An optical torque sensor for robotic applications," *Int. J. Optomechatronics*, vol. 7, no. 4, pp. 263–282, Oct. 2013.
- [46] Y. Noh, S. Sareh, J. Back, H. A. Würdemann, T. Ranzani, E. L. Secco, A. Faragasso, H. Liu, and K. Althoefer, "A three-axial body force sensor for flexible manipulators," in *Proc. IEEE Int. Conf. Robot. Autom. (ICRA)*, May 2014, pp. 6388–6393.
- [47] Y. Noh, J. Bimbo, S. Sareh, H. Wurdemann, J. Fraš, D. Chaturanga, H. Liu, J. Housden, K. Althoefer, and K. Rhode, "Multi-axis force/torque sensor based on simply-supported beam and optoelectronics," *Sensors*, vol. 16, no. 11, p. 1936, Nov. 2016.
- [48] Y. Noh, J. Bimbo, A. Stilli, H. Wurdemann, H. Liu, J. Housden, K. Rhode, and K. Althoefer, "A new miniaturised multi-axis force/torque sensors based on optoelectronic technology and simply-supported beam," in *Proc. IEEE/RSJ Int. Conf. Intell. Robots Syst. (IROS)*, Oct. 2016, pp. 202–207.
- [49] Everlight. *ITR 8307 Reflective IR Opto Switch*. Accessed: Mar. 17, 2020. [Online]. Available: <https://everlighteurope.com/optical-switch/253/ITR8307L24TR8.html>
- [50] *ITR 9904 Reflective IR Opto Switch*. Accessed: Mar. 17, 2020. [Online]. Available: <https://everlighteurope.com/optical-switch/262/ITR9904.html>
- [51] Vishay Semiconductors. *TCST-1103 Photo Interrupter*. Accessed: Mar. 17, 2020. [Online]. Available: <http://www.vishay.com/optical-sensors/list/product-83764/>
- [52] Arduino. *Arduino Website*. Accessed: Mar. 9, 2020. [Online]. Available: <https://www.arduino.cc>
- [53] PJRC Inc. *Teensy USB Development Board*. Accessed: Mar. 9, 2020. [Online]. Available: <https://www.pjrc.com/teensy/>
- [54] Vishay Semiconductors. *Proximity Sensors With Interrupt, IRED, and I2C Interface*. Accessed: Mar. 7, 2020. [Online]. Available: <http://www.vishay.com/docs/84917/vcnl3040.pdf>
- [55] Silicon Labs. *Si115x Proximity and Ambient Light Sensor IC With I2C Interface*. Accessed: Mar. 10, 2020. [Online]. Available: <https://www.silabs.com/sensors/optical/si115x>
- [56] A. E. H. Love, *A Treatise on the Mathematical Theory of Elasticity*. Cambridge, U.K.: Cambridge Univ. Press, 1942.
- [57] J. A. Haringx, "Elastic stability of flat spiral springs," *Appl. Sci. Res.*, vol. 2, no. 1, pp. 9–30, Jan. 1951.
- [58] J.-S. Chen and I.-S. Chen, "Deformation and vibration of a spiral spring," *Int. J. Solids Struct.*, vols. 64–65, pp. 166–175, Jul. 2015.
- [59] L. Xie, P. Ko, and R. Du, "The mechanics of spiral springs and its application in timekeeping," *J. Appl. Mech.*, vol. 81, no. 3, Mar. 2014, Art. no. 034504.
- [60] H. K. Obermeyer, F. H. Obermeyer, and L. Obermeyer. (Jan. 2012). *Multi-Axis Joystick and Transducer Means Therefore*. [Online]. Available: <https://patents.google.com/patent/US8094121zh>
- [61] A. Ahmed and H. Zhou, "Synthesis of nonlinear spiral torsion springs," *Int. J. Eng. Res. Technol.*, vol. 3, no. 6, pp. 4–10, 2014.
- [62] *OpenSCAD*. Accessed: Aug. 15, 2016. [Online]. Available: <http://www.openscad.org/>
- [63] M. Quigley, K. Conley, B. Gerkey, J. Faust, T. Foote, J. Leibs, R. Wheeler, and A. Y. Ng, "ROS: An open-source robot operating system," in *Proc. ICRA Workshop Open Source Softw.*, May 2009, vol. 3, no. 3.2, p. 5.
- [64] S. Cousins, "ROS on the PR2 [ROS Topics]," *IEEE Robot. Autom. Mag.*, vol. 17, no. 3, pp. 23–25, Sep. 2010.
- [65] P. Watson and S. Drake, "Pedestal and wrist force sensors for automatic assembly," in *Proc. 5th Int. Symp. Ind. Robots*, 1975, pp. 501–511.
- [66] R. M. Voyles, J. D. Morrow, and P. K. Khosla, "The shape from motion approach to rapid and precise force/torque sensor calibration," *J. Dyn. Syst., Meas., Control*, vol. 119, no. 2, pp. 229–235, Jun. 1997.
- [67] K. Kim, Y. Sun, R. M. Voyles, and B. J. Nelson, "Calibration of multi-axis MEMS force sensors using the shape-from-motion method," *IEEE Sensors J.*, vol. 7, no. 3, pp. 344–351, Mar. 2007.
- [68] F. Bagge Carlson, "On the calibration of force/torque sensors in robotics," 2019, *arXiv:1904.06158*. [Online]. Available: <http://arxiv.org/abs/1904.06158>
- [69] T. E. Oliphant, *A Guide to NumPy*. Spanish Fork, UT, USA: Trelgol Publishing, 2006.
- [70] S. C. C. S. van der Walt, S. C. Colbert, and G. Varoquaux, "The NumPy array: A structure for efficient numerical computation," *Comput. Sci. Eng.*, vol. 13, no. 2, pp. 22–30, Mar. 2011.
- [71] P. Virtanen et al., "SciPy 1.0: Fundamental algorithms for scientific computing in python," *Nature Methods*, vol. 17, pp. 261–272, 2020.
- [72] A. E. Hoerl and R. W. Kennard, "Ridge regression: Biased estimation for nonorthogonal problems," *Technometrics*, vol. 12, no. 1, pp. 55–67, Feb. 1970.
- [73] R. Tibshirani, "Regression shrinkage and selection via the lasso," *J. Roy. Stat. Soc. B, Methodol.*, vol. 58, no. 1, pp. 267–288, Jan. 1996.
- [74] P. J. Huber, "Robust estimation of a location parameter," *Ann. Math. Statist.*, vol. 35, no. 1, pp. 73–101, Mar. 1964, doi: 10.1214/aoms/1177703732.
- [75] F. Wasserfall, N. Hendrich, F. Fiedler, and J. Zhang, "3D-printed low-cost modular force sensors," in *Proc. 20th Int. Conf. Climbing Walking Robots (CLAWAR)*, 2017, pp. 485–492.
- [76] N. Hendrich and A. Bernardino, "Affordance-based grasp planning for anthropomorphic hands from human demonstration," in *Proc. 1st Iberian Robot. Conf. (ROBOT)*. Cham, Switzerland: Springer, 2014, pp. 687–701.
- [77] ATI Industrial Automation Inc. *FT Sensor: Nano 17*. Accessed: Mar. 11, 2020. [Online]. Available: https://www.ati-ia.com/products/ft/ft_models.aspx?id=Nano17



NORMAN HENDRICH received the B.Sc. and M.Sc. degrees in physics and the Ph.D. degree in computer science from the University of Hamburg, Germany, in 1986, 1991, and 1996, respectively. He is currently a Senior Lecturer with the Department of Informatics, University of Hamburg. He has participated as a Principal Investigator in several collaborative European research projects and also acts as a Project Manager of the joint Sino-German project Transregio-SFB TRR169 Crossmodal Learning. His research interests include computer simulation and machine learning, with a focus on applications in service robotics and dexterous manipulation.



FLORENS WASSERFALL received the B.Sc. degree in computer science with a minor in oceanography in 2009, started working with 3D-printers, in 2011, the M.Sc. degree in adaptive slicing algorithms for FFF-printing, in 2014, and the Ph.D. degree from the University of Hamburg, presenting design software for the integration of electronics and sensors into 3D-printed parts. He is currently a Postdoctoral Research Associate with the Department of Informatics, University of Hamburg. His research interests include slicing and design algorithms for hybrid additive manufacturing and their application in the field of robotics. He teaches courses in computer architecture and applied robotics.



JIANWEI ZHANG (Member, IEEE) received the Bachelor of Engineering (Hons.) and Master of Engineering degrees from the Department of Computer Science, Tsinghua University, Beijing, China, in 1986 and 1989, respectively, the Ph.D. degree from the Department of Computer Science, Institute of Real-Time Computer Systems and Robotics, University of Karlsruhe, Germany, in 1994, and the Habilitation degree from the Faculty of Technology, University of Bielefeld, Germany, in 2000. He is currently a Professor and the Director of the group TAMS, Department of Informatics, University of Hamburg, Germany. His research interests are sensor fusion, intelligent robotics, and multimodal machine learning. In these areas, he has published about 400 journal and conference papers, technical reports, and four books. He received multiple best paper awards. He is the coordinator of the DFG/MSFC Transregional Collaborative Research Centre SFB/TRR169 Crossmodal Learning and several EU robotics projects. He is life-long Academician of the Academy of Sciences in Hamburg. He was a member of the IEEE Robotics and Automation Society AdCom, from 2013 to 2015. He is the General Chair of IEEE MFI 2012, IEEE/RSJ IROS 2015, and the International Symposium of Human-Centered Robotics and Systems 2018.

...